Available online at www.sciencedirect.com

ScienceDirect

Geochimica et Cosmochimica Acta 197 (2017) 71–86

Geochimica et Cosmochimica Acta

www.elsevier.com/locate/gca

Effects of grain size, mineralogy, and acid-extractable grain coatings on the distribution of the fallout radionuclides ^{7}Be, ^{10}Be, ^{137}Cs, and ^{210}Pb in river sediment

Adrian A. Singleton [a], Amanda H. Schmidt [a,*], Paul R. Bierman [b], Dylan H. Rood [c,d,e], Thomas B. Neilson [b], Emily Sophie Greene [b], Jennifer A. Bower [b], Nicolas Perdrial [b]

[a] *Oberlin College, Geology Department, Oberlin, OH 44074, USA*
[b] *University of Vermont, Department of Geology, Burlington, VT 05405-1758, USA*
[c] *Department of Earth Science and Engineering, Imperial College London, South Kensington Campus, London SW7 2AZ, UK*
[d] *Accelerator Mass Spectrometry Laboratory, Scottish Universities Environmental Research Centre, East Kilbride G75 0QF, UK*
[e] *Earth Research Institute, University of California, Santa Barbara, CA 93016, USA*

Received 23 February 2016; accepted in revised form 10 October 2016; available online 19 October 2016

Abstract

Grain-size dependencies in fallout radionuclide activity have been attributed to either increase in specific surface area in finer grain sizes or differing mineralogical abundances in different grain sizes. Here, we consider a third possibility, that the concentration and composition of grain coatings, where fallout radionuclides reside, controls their activity in fluvial sediment. We evaluated these three possible explanations in two experiments: (1) we examined the effect of sediment grain size, mineralogy, and composition of the acid-extractable materials on the distribution of ^{7}Be, ^{10}Be, ^{137}Cs, and unsupported ^{210}Pb in detrital sediment samples collected from rivers in China and the United States, and (2) we periodically monitored ^{7}Be, ^{137}Cs, and ^{210}Pb retention in samples of known composition exposed to natural fallout in Ohio, USA for 294 days.

Acid-extractable materials (made up predominately of Fe, Mn, Al, and Ca from secondary minerals and grain coatings produced during pedogenesis) are positively related to the abundance of fallout radionuclides in our sediment samples. Grain-size dependency of fallout radionuclide concentrations was significant in detrital sediment samples, but not in samples exposed to fallout under controlled conditions. Mineralogy had a large effect on ^{7}Be and ^{210}Pb retention in samples exposed to fallout, suggesting that sieving sediments to a single grain size or using specific surface area-based correction terms may not completely control for preferential distribution of these nuclides.

We conclude that time-dependent geochemical, pedogenic, and sedimentary processes together result in the observed differences in nuclide distribution between different grain sizes and substrate compositions. These findings likely explain variability of measured nuclide activities in river networks that exceeds the variability introduced by analytical techniques as well as spatial and temporal differences in erosion rates and processes. In short, we suggest that presence and amount of pedogenic grain coatings is more important than either specific surface area or surface charge in setting the distribution of fallout radionuclides.

Keywords: Sediment tracers; Metal adsorption; Cosmogenic; Sediment fingerprinting

* Corresponding author.
E-mail address: aschmidt@oberlin.edu (A.H. Schmidt).

http://dx.doi.org/10.1016/j.gca.2016.10.007
0016-7037/

1. INTRODUCTION

Tracing and quantifying sediment movement improves the understanding of Earth surface processes (Dietrich et al., 1982) and their interplay with diverse drivers including tectonics (Zeitler et al., 2001), climate (Reiners et al., 2003), and human activity (Hooke, 2000). Quantitative geochemical techniques are increasingly employed for sediment analysis (Guzmán et al., 2013). For example, the fallout radionuclides (FRNs) ^{7}Be ($t_{1/2} = 53$ d), meteoric ^{10}Be ($^{10}Be_m$; $t_{1/2} = 1.4$ My), ^{137}Cs ($t_{1/2} = 30.2$ y), and unsupported ^{210}Pb ($^{210}Pb_{ex}$; $t_{1/2} = 22.3$ y) have been used to estimate erosion rates (Brown et al., 1988; Walling et al., 1999; Matisoff and Whiting, 2012) and to trace sediment sources (Wallbrink and Murray, 1993; Reusser and Bierman, 2010; Belmont et al., 2014; Hancock et al., 2014; Smith and Blake, 2014).

Grain-size dependent variability in FRN concentration has been widely observed in both soils and detrital sediment samples (e.g., He and Walling, 1996; Wittmann et al., 2012; Smith and Blake, 2014; Taylor et al., 2014) and is generally attributed to variations either in specific surface area (He and Walling, 1996; Wittmann et al., 2012; Taylor et al., 2014) or varying mineralogy (Tamura, 1963; Aldahan et al., 1999; Nakao et al., 2014). A third possibility that may also explain observed grain size dependencies is that FRN concentration is a function of grain-coatings (Greene, 2016). Although FRN systems are well-understood in soils (Parsons and Foster, 2011, 2013; Mabit et al., 2013), grain-size dependent variability in nuclide activity of detrital sediments is less frequently studied (Brown et al., 1988; Wallbrink and Murray, 1993; Mabit et al., 2008; Belmont et al., 2014; Hancock et al., 2014).

In this paper, we compare grain size, mineralogy, and composition of acid-extractable materials to the distribution of FRNs (primarily ^{10}Be and ^{210}Pb) in detrital sediment in order to understand better observed grain size dependencies. We do this by measuring nuclide activities in different size fractions of detrital fluvial sediment, and measuring change in nuclide activity over time in a controlled natural fallout experiment with sediment of known grain size and composition. We then quantify the composition of acid-extractable materials as a proxy for the grain coatings in which these nuclides reside using X-ray diffraction (XRD), portable X-ray fluorescence (pXRF), and inductively coupled plasma spectrometry (ICP-OES).

2. BACKGROUND

Fallout radionuclides have different sources. ^{7}Be and $^{10}Be_m$ are cosmogenic isotopes created by cosmic-ray induced spallation in the atmosphere (Papastefanou and Ioannidou, 1996). $^{210}Pb_{ex}$ is created in the atmosphere by decay of ^{222}Rn (from ^{238}U decay series) that has escaped from Earth materials as a gas (Appleby et al., 1986). ^{137}Cs is an anthropogenic radionuclide. Its presence in sediment is largely the result of atmospheric nuclear weapons testing during the 1960s, with later and less significant releases from accidents at nuclear power plants after atmospheric testing ceased (Matisoff and Whiting, 2012). After formation or release, FRNs strongly bind to aerosols (Papastefanou and Ioannidou, 1996; Likuku and Branford, 2011; Kristiansen et al., 2012), which are primarily deposited via precipitation in all but the most arid regions, where dry fall dominates (Ioannidou and Papastefanou, 2006). FRNs can be reworked and redeposited as dust by aeolian transport, changing apparent nuclide deposition rates (Ouimet et al., 2015).

Many studies report grain-size dependent distributions of trace metals, including FRNs, with higher concentrations in fine-grained fractions of sediments and soils (e.g., He and Walling, 1996; Wittmann et al., 2012; Smith and Blake, 2014; Taylor et al., 2014), although some studies (e.g., Brown et al., 1988) show little if any grain size effect on FRN concentration in fluvial sediment. Prior research suggests two explanations for preferential FRN distribution that are not mutually exclusive: (1) FRNs are sorbed to particles in proportion to specific surface area, so finer sediment fractions accumulate more nuclides per unit mass (He and Walling, 1996; Wittmann et al., 2012; Taylor et al., 2014); and (2) FRNs are preferentially sorbed to specific minerals (Tamura, 1963; Aldahan et al., 1999; Nakao et al., 2014), and thus finer sediment fractions have higher nuclide activity due to grain-size dependent prevalence of such minerals. Typically, grain size dependencies are accounted for by sieving sediment to a particular grain size (usually <63 μm, though sometimes as small as <10 μm or even <2 μm), limiting analysis to suspended sediment (c.f., Guzmán et al., 2013), or applying a correction factor based on specific surface area (e.g., He and Walling, 1996). The usefulness of specific surface area correction factors is debated (Smith and Blake, 2014). Furthermore, Kaste et al. (2014) found that 100% of ^{7}Be delivered in rainfall was adsorbed to gravel in a natural delivery experiment, suggesting that coarse grained materials do adsorb some FRNs.

The presence of competing cations may affect the degree of sorption as well (Srivastava et al., 2005). Beryllium may compete with Al^{3+} and Ca^{2+} for sorption sites (Bhat et al., 2005; Graly et al., 2010; Willenbring and von Blanckenburg, 2010). Similarly, Cs competes with K (Steefel et al., 2003; Fuller et al., 2014) and Pb competes with other heavy metals (Covelo et al., 2007; Seo et al., 2008). Much of the ^{7}Be and $^{210}Pb_{ex}$ in soils and sediments may be bound to, or co-precipitated with, Fe–Mn-(hydr) oxides (Jia et al., 2006). While Wittmann et al. (2012) find that the majority of the $^{10}Be_m$ inventory in Amazon River bed sediment had co-precipitated with authigenic amorphous and crystalline Fe–Mn-(hydr)oxides, a global meta-analysis of $^{10}Be_m$ data showed that $^{10}Be_m$ distribution can be proportional to a variety of soil characteristics but that no single parameter dominates (Graly et al., 2010). Others have found that $^{10}Be_m$ may eventually become incorporated into authigenic clays (Barg et al., 1997). Fe and Mn phases often form as grain coatings during pedogenesis (Stoops et al., 2010), suggesting that the composition and concentration of grain coatings is likely to be an important factor in FRN retention by sediment. Here, we test that suggestion. Although some have found that organic matter is a

potential control on FRN activity (e.g., Smith and Blake, 2014), others have found that organic matter only accounts for a small percentage of the variability in $^{10}Be_m$ activity in samples and that grain coatings are more important for FRN retention (Barg et al., 1997; Wittmann et al., 2012; Greene, 2016).

Using the assumption that stable ^{9}Be behaves in a geochemically similar manner to $^{10}Be_m$, ^{9}Be has been used to correct for preferential distribution of $^{10}Be_m$ (e.g., Bacon et al., 2012; von Blanckenburg et al., 2012; Wittmann et al., 2012). The method appears to normalize against grain size dependencies because ^{9}Be concentration has similar grain size dependencies as $^{10}Be_m$ concentration (Wittmann et al., 2012).

3. METHODS

We conducted two different experiments to evaluate the effect of varying mineralogy, grain size, composition and mass of acid extractable materials of sediments on the distribution of ^{7}Be, $^{10}Be_m$, ^{137}Cs, and $^{210}Pb_{ex}$. In one experiment we measured the concentration of ^{7}Be, $^{10}Be_m$, ^{137}Cs, and $^{210}Pb_{ex}$ in five grain sizes of detrital river sediment from the Mekong River watershed in Yunnan, China, and the Vermilion River in Ohio, USA (Fig. 1). In a separate natural delivery experiment designed to show end-member behavior of materials of consistent composition and/or grain size, we monitored the retention of $^{210}Pb_{ex}$, ^{137}Cs, and ^{7}Be in five grain sizes each of quartz and river sediment as well as five phyllosilicates; these samples were exposed outside in Ohio to natural fallout, including dryfall and rainfall, for 294 days. We determined total sediment elemental and mineralogical composition (substrate plus grain coating) via microscopy, quantitative powder X-ray diffraction (XRD), and portable X-ray fluorescence (pXRF) for all samples in both experiments. We used acid extraction to determine the elemental make up and mass of HCl-extractable materials as a proxy for grain coatings (Greene, 2016).

3.1. Detrital samples

We collected fluvial bed sediment samples from the active channel at six sites in Yunnan, China in January 2014 and three sites in Ohio, USA in April and May 2015 (Figs. 1 and 2). All sample sites in China were located in two tributary catchments of the Mekong River watershed, the Weiyuan River (CH-116, 17 km^2; CH-114, 1445 km^2; CH-117, 2508 km^2) and Nankai River (CH-121, 38 km^2; CH-122, 487 km^2; CH-127, 1006 km^2). Ohio sites are located on tributaries to the Vermilion River (V-005, 88 km^2; V-006, 90 km^2; V-007, 6.4 km^2). All three watersheds are predominately agricultural landscapes. The Weiyuan watershed is ~23% agriculture, concentrated near valley bottoms and including grain and tobacco plantations, with forests on upland locations (Neilson, 2015). The Nankai watershed is >50% agricultural with tea and rubber plantations on upland locations and rice and sugar

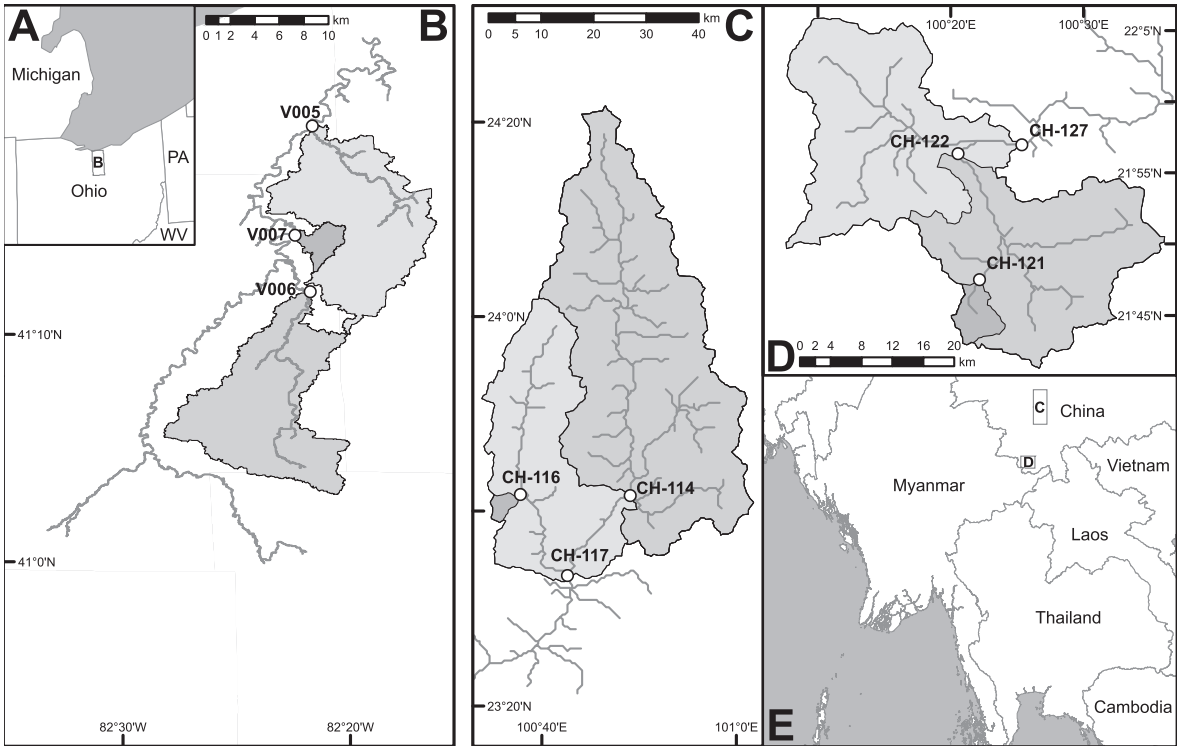

Fig. 1. Maps of the two study regions. We collected detrital samples in five grain sizes from three sites in the Vermilion River catchment, Ohio (A, B) and from three sites each in two basins (Weiyuan (C) and Nankai (D)) in the Mekong River catchment in Yunnan, China (E). Sampling locations are labeled by white circles on the maps.

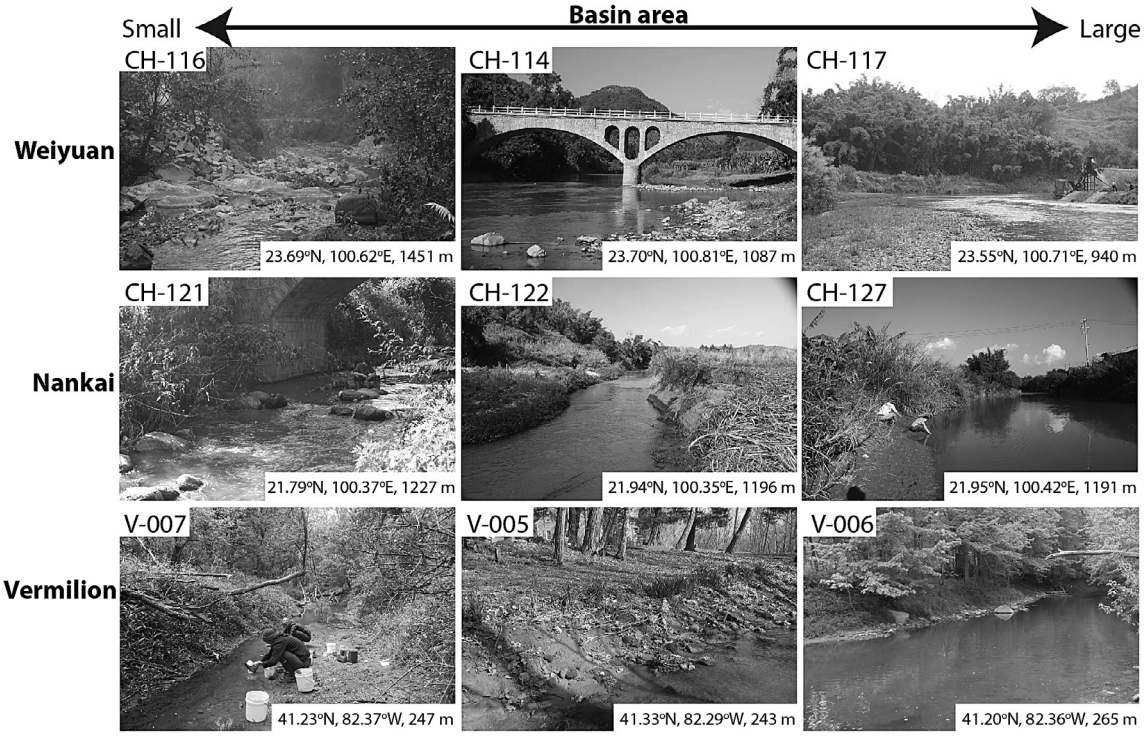

Fig. 2. Photos of field sites. From top to bottom: sampling sites in the Weiyuan, Nankai, and Vermilion Rivers; from left to right: the headwater, intermediate, and outlet sites for each basin. Yunnan samples are from the Weiyuan and Nankai Rivers. Sample names in upper left. GPS coordinates (WGS84) and sample collection elevation in lower right. See Fig. 1 for how watersheds in each basin are related to one another. Note that the Vermilion samples are all taken from tributaries to the Vermilion River, so the largest watershed has an outlet that is higher elevation than the smaller ones.

cane paddies in lowland locations (Neilson, 2015). The Vermilion watershed is dominated by soy and corn monoculture farms with significant subsurface drainage tiles.

Sampling procedures were identical at all nine sites: we wet-sieved the detrital bed material samples into five grain sizes (<63 μm, 63–125 μm, 125–250 μm, 250–500 μm, 500–850 μm) in the field. At each site we also collected bulk sediment and, for all samples, sieved more sediment in the lab using deionized water to ensure enough material for decay counting. Table SI1 details which samples were used for which analyses, where they were sieved, and what grain size they contained.

3.2. Sediment composition

We embedded the >63 μm fractions of the samples in epoxy, prepared thin-section slides, and examined them using polarized light microscopy in order to determine their composition. We also examined the clay mineralogy for these samples via pXRD of the <2 μm fraction, which we obtained by centrifuging the <63 μm fraction (USGS, 2001). For each sample, we collected diffraction patterns three times: once as a random powder mount, once oriented flat on glass slides via the "filter peel" method using vacuum filtration, and once after a minimum of 8 h of ethylene glycol solvation using the oriented slide, following procedures outlined by Moore and Reynolds (1997). Diffraction patterns were collected at Oberlin College on a Rigaku Ultima IV X-ray Diffractometer from 2° to 65° 2θ with a step width of 0.02° and a counting time of 0.5 s per step using Cu K_α radiation.

We collected bulk-elemental composition for each sample via pXRF. Samples were powdered in a shatterbox for 60 s (repeated until cleavage was no longer visible) in a steel vessel, packed in containers with polyethylene thin film windows, and measured for 33 elements under He atmosphere with a 90-s counting time on a Thermo Scientific Niton XL3t 900 Series portable XRF on low, medium, and light-element settings at the University of Vermont. The accuracy of the quantitative results of each element was addressed by regularly analyzing certified NIST 2780 and TILL-4 standards. Only elements for which the standards values were within 5% of the certified values are reported. We used the error-weighted average of duplicate measurements.

In order to understand the relationship between composition and quantity of grain coatings and the activity of FRNs, we quantified the composition of acid-extractable materials in the samples. The composition and mass of acid-extracted materials was measured using Inductively Coupled Plasma Optical Emission Spectrometry (ICP-OES) at the University of Vermont. Powdered samples were leached in warm 6 M HCl for 24-h in an ultrasonic bath, and the leachate was analyzed (see Supporting text and Figs. SI1–4) (Greene, 2016). We measured Be, Na, Mg, Al, Si, K, Ca, Mn, Ti, and Fe. Lab replicates of samples

leached at separate times and then analyzed by ICP-OES reproduce well (<0.5%) (Greene, 2016). The HCl-leach we use is significantly stronger than anything occurring naturally and is not designed to mimic natural processes but instead to remove all pedogenic coatings from samples to quantify their mass and composition while not affecting substrate materials (Snape et al., 2004). Using stable ^{9}Be measured in the HCl-leachate, we normalized $^{10}Be_m$ activities for the Yunnan samples following the approach of von Blanckenburg et al. (2012).

The identities of crystalline phases dissolved in the acid-extraction are an important part of the composition of grain coatings. To understand better which crystalline phases are dissolved in the acid extraction, the <63 μm fraction of samples CH-114, CH-116, CH-121, CH-122, V-005, and V-007 was analyzed by X-ray diffraction before and after HCl extraction. Diffractograms were acquired at the University of Vermont on a Rigaku Miniflex II diffractometer equipped with a Cu K_α radiation source ($\lambda = 1.54$ Å) operated at 30 kV and 15 mA. Samples were randomly mounted on glass holders and scanned from 3° to 65° 2θ at 0.02° 2θ steps and 1° per minute. Quantitative analysis of X-ray diffractograms was performed with the Rietveld module in the X'Pert HighScore Plus software. After initial background manual subtraction and qualitative analysis, phase mixtures extracted from the literature as well as the AMCSD and COD databases (Downs and Hall-Wallace, 2003; Gražulis et al., 2009, 2012) were modeled for scale factor, preferred orientation and peak shape (including March-Dollase factor). According to the Highscore Plus Manual, the detection limit is 0.5%.

3.3. Measuring $^{10}Be_m$

To measure $^{10}Be_m$ (done only for the Yunnan samples), sediment was powdered, ^{9}Be carrier added, and beryllium extracted at the University of Vermont following a modified version of the flux/fusion procedure of Stone (1998). Samples were analyzed by Accelerator Mass Spectrometry (AMS) at the Scottish Universities Environmental Research Centre in East Kilbride, Scotland (Xu et al., 2010, 2015) and normalized to the NIST standard with an assumed $^{10}Be/^{9}Be$ ratio of 2.79×10^{-11} (Nishiizumi et al., 2007). Background correction was done using process blanks run with each batch of 16 samples; the final uncertainty of the ratio is the uncertainty of the isotopic measurement and the blank propagated in quadrature. Table SI2 has AMS data for all samples analyzed for $^{10}Be_m$. In another study on samples from the same area processed at the same time, lab replicates reproduced results within <3% error (Sosa-Gonzalez et al., 2015).

3.4. Measuring ^{7}Be, ^{137}Cs, and $^{210}Pb_{ex}$

We decay counted a mix of field- and lab-sieved sample material (2.3–226.2 g, mean 40.5 g, standard deviation 37.8 g, see Table SI1) to analyze activity of ^{7}Be, ^{137}Cs, and $^{210}Pb_{ex}$. After sieving, samples were dried in an oven then packed in air-tight plastic beakers with screw top lids; sample mass and thickness in beaker were recorded. Beakers were additionally sealed with electrical tape. After sealing, samples sat for at least 20 days to allow for radon ingrowth; this allowed us to determine supported ^{210}Pb activity by measuring daughter products of ^{222}Rn (Appleby et al., 1986; Murray et al., 1987). This method over-estimates supported ^{210}Pb because it assumes that all ^{222}Rn gas in the rock decays to ^{210}Pb, but we know that some percentage must escape because there is unsupported ^{210}Pb in sediment (Graustein and Turekian, 1990; Greeman and Rose, 1996; Du and Walling, 2012).

We used a semiconductor detector efficiency calculation software, Angle, to determine detector efficiency for each sample. Angle combines theoretical and empirical calibrations for gamma detector efficiency to allow for more flexibility in sample geometry and composition (Jovanovic et al., 2010). In order to use Angle to determine detector efficiency for each sample, we defined the detector parameters, beaker geometry, and created a reference efficiency curve using a calibrated standard. The calibrated standard is a 0.1 μCi activity mixed gamma standard, including ^{210}Pb and ^{137}Cs, in an epoxy matrix purchased in January 2012 from Eckert and Ziegler. Samples vary in thickness, calculated density, and composition. We measured thickness and mass for each sample and used that to determine density for Angle. Sample composition was determined for each sample using portable X-ray Fluorescence at the University of Vermont. Table SI3 shows the composition information for each sample. Table SI4 shows the sample geometry for each sample, including mass, thickness, density as well as the Angle output for each sample.

Angle does not report errors. To determine errors in Angle, we first cross-checked our calibrations and reference energy curve on one known standard (3 μCi), also in an epoxy matrix and purchased from Eckert and Ziegler in January 2012. This error was minimal (<3%). In addition, we ran Angle for different end-member compositions of samples ranging from quartz to raw granite and determined that changes in composition have a minimal effect on higher energy decays but a relatively large effect on low energy decays. Having composition data minimizes this error, but to be conservative, we consider Angle-derived efficiency to have 5% errors for all energies. Table SI5 shows the Angle output for each energy for each sample.

Samples were counted at Oberlin College for 24–168 h (most samples were counted for 24 or 96 h) in a Canberra high-purity broad energy germanium detector (HP BEGe). For each of eight peaks of interest associated with ^{210}Pb (46.5 keV), ^{7}Be (477.6 keV), ^{137}Cs (661.7 keV), ^{214}Pb (295.2 and 351.9 keV) and ^{214}Bi (609.3, 1120.3, and 1764.5 keV), net peak area, corrected for both background of an empty sample beaker counted for 96 h and continuum, for each isotope were determined by Canberra's Genie2000 software (http://www.canberra.com/products/radiochemistry_lab/genie-2000-software.asp). Peak regions were identified using regions of interest we defined prior to analysis of any samples. Peak region definition was based on peak widths in known standards and extrapolated for peaks not in the standard using the equations in Practical Gamma-ray Spectrometry (Gilmore, 2011). The error in peak fitting is not known. Table SI6 shows the energy,

energy range used for peak area, gamma yield at that energy, and half-life for each radionuclide. Table SI7 shows the output for each sample from Genie2000.

To control for machine drift, we measured a quality control standard for 600 s prior to counting each sample. If the quality control showed drift in the relationship between multi-channel analyzer channels and decay energy, we recalibrated the energy to channel relationship before proceeding with further sample analysis.

We determined the critical limit (L_C) for the detector for each energy and each sample using the continuum counts (B) for the area immediately surrounding that energy to ensure 95% confidence that the peak area is significantly different from the continuum (Eq. (1)).

$$L_C = 2.33\sqrt{B} \tag{1}$$

To determine activity of each isotope (A), we used Eq. (2):

$$C = A\varepsilon tP \tag{2}$$

where C is the counts in the peak area, ε is the detector efficiency at that energy for that sample, t is the time counted (in seconds), and P is the probability of decays at that energy. Occasionally, net peak areas after subtracting the continuum are reported by the detector as negative. Negative numbers reflect noise in the continuum and are treated as zero peak areas.

To determine percent error in sample activity, we added the percent errors contributing to sample activity in quadrature. These errors are error in peak area as determined by Genie 2000 for the Poisson counting statistics and error in detector efficiency determined from Angle (5%). Errors in peak area fitting are not included. Error in probability of decays and measurement time are insignificant compared to other errors. Genie2000 reports three significant figures, so all calculations were done with three significant figures. Errors in ^{7}Be are likely underestimated due to not accounting for interferences from ^{214}Pb and ^{228}Ac lines (Landis et al., 2012).

The activity for ^{137}Cs and ^{7}Be was determined directly from Eq. (2) for samples with significant peak areas of ^{137}Cs and ^{7}Be. Because ^{137}Cs is no longer being deposited and is decaying in all locations, we corrected for isotope decay to a standard date for all samples – 1/1/2005; this correction controls for different sampling times for each sample. We observed negligible ^{137}Cs delivery in our natural delivery experiment, which supports this assumption. ^{7}Be is still being deposited, thus activity was corrected to the sample collection date. After correcting activity for decay, we divided activity by the mass of the sample to determine the activity per kg [Bq/kg]; errors in mass were insignificant compared to other errors and were thus not included in error calculations. Yunnan samples were in transit from China for too long to quantify ^{7}Be in them; thus, ^{7}Be was only measured in Ohio samples.

To determine $^{210}Pb_{ex}$ we subtracted supported ^{210}Pb from total ^{210}Pb:

$$^{210}Pb_{ex} = {}^{210}Pb_{total} - {}^{210}Pb_{supported} \tag{3}$$

Total ^{210}Pb activity was determined directly from Eq. (2). To determine supported ^{210}Pb, we used Eq. (2) to calculate apparent supported ^{210}Pb for each of the five energies of the two daughter products of ^{222}Rn (295.22 (^{214}Pb), 351.93 (^{214}Pb), 609.31 (^{214}Bi), 1120.3 (^{214}Bi), 1764.5 (^{214}Bi) keV) (Fig. SI5). After doing an analysis of all five proxies for supported ^{210}Pb for all samples, we determined that the estimates calculated using 295.22 (^{214}Pb), 351.93 (^{214}Pb), and 609.31 (^{214}Bi) keV have the lowest percent errors and the most consistent estimates for supported ^{210}Pb activity. Therefore, we used the weighted mean and weighted error of estimated supported ^{210}Pb derived from activity at these energies to determine supported ^{210}Pb for each sample. Table SI8 shows the activity of total and supported ^{210}Pb for each sample. We show all five estimates for supported ^{210}Pb as well as the weighted average and error used for further calculations.

Error in $^{210}Pb_{ex}$ is the sum in quadrature of the absolute error in the total and supported ^{210}Pb terms. Thus, because we are subtracting the two numbers to determine $^{210}Pb_{ex}$ but adding the errors, the percent error in $^{210}Pb_{ex}$ quickly can become large. Ultimately, our detection limit depends on the ratio of $^{210}Pb_{ex}$ to supported ^{210}Pb. We modeled the fraction error using the average error in our supported and total ^{210}Pb measurements and find that at ratios around 2×10^{-3}, we cannot reliably detect $^{210}Pb_{ex}$ (Fig. SI6). This is a more important issue in watersheds with more igneous rocks than those with more sedimentary rocks, because basins with more igneous rocks tend to have higher supported ^{210}Pb. To be 95% confident that our $^{210}Pb_{ex}$ is greater than 0, we need the error to be <61% (for a one-tailed distribution, $1.645\sigma = 0.05$). Therefore, we consider samples with errors >61% to be below the detection limit for $^{210}Pb_{ex}$.

3.4.1. Natural delivery experiment

In order to explore the relative effects of grain size and sample composition on the retention of FRNs in sediment, we used a natural delivery experiment where pure mineral phases and river sediment samples received fallout. We monitored the retention of naturally delivered fallout outdoors in fifteen samples contained in filter-bottomed, freely draining PTFE beakers (500 ml internal volume, Savillex part number 100-0500-03) for 294 non-continuous days over a period of ~18 months. PTFE was used to minimize adhesion of nuclides to container surfaces. Samples were located ~6 inches off the ground in a ground-level restricted-access courtyard of the Science Center at Oberlin College (Fig. 3).

Each container was partially filled (22.9–268.2 g) with one of five grain sizes each (<63 μm, 63–125 μm, 125–250 μm, 250–500 μm, 500–850 μm) of quartz (obtained from Global Drilling Suppliers, Inc.) and river sediment (a mix of samples 05-3R-4-MEK, 05-3R-11b-SAL, and 06-3R-29-MEK from Henck et al. (2011)) or five phyllosilicate mineral powders (kaolinite, illite, muscovite, vermiculite, and montmorillonite) obtained from Ward's Scientific and VWR International (see Table SI9 for details on exactly what was in each container). The bottom of each sample container was lined with a 5–6 μm (<63 μm fraction

Fig. 3. Samples in the restricted-access courtyard (41.29°N, 82.22° W, 247 m). The top row, from left to right, is: kaolinite, illite, muscovite, vermiculite, and montmorillonite. The middle row, from left to right, is quartz sand <63, 63–125, 125–250, 250–500, and 500–850 μm. The bottom row, from left to right, is river sand <63, 63–125, 125–250, 250–500, and 500–850 μm. The single container on the far left between the top and middle rows is the rainfall beaker where we collected rainfall during each period. A rain gauge is to the left of the apparatus (outside of the photo) next to the middle row of containers.

and sheet silicates) or 30–40 μm (all other samples) pore size PTFE filter (Savillex part numbers 450-90-4 & 450-90-6). During periods of precipitation, if any container filled with water might overflow if it received more rain, all containers were capped to ensure that delivery of fallout nuclides was as equal as possible among the samples; they were uncapped once the weather cleared. Although this means that samples received less fallout than was delivered during the time period, they were all exposed to identical flux of fallout. The containers were arranged in a ~1 m^2 matrix, placed closely together to minimize spatial variation in fallout delivery (Fig. 3). Before placing the samples outside, we collected the gamma spectrum of the containers with the added samples. Five times during the experiment (exposure days 33, 96, 155, 179, 294), all samples were brought inside, dried in a warm oven (~50 °C) and measured for change in total ^{210}Pb and ^{7}Be activities (see Table SI10 for exact dates samples were exposed and characteristics of the rain events). The total time for indoor sample treatment and analysis was 33–43 days; the time varied by measurement period but was the same for all samples. The time indoors before counting some samples as well as the time outdoors is on the same order of magnitude as a half-life of ^{7}Be, and the concurrent addition from rainfall and decay of ^{7}Be increases our errors for this isotope. Samples received a total of 812 mm of rain over the course of the experiment. All data, including efficiency, composition, and counts, related to gamma spectrometry of the natural delivery samples are shown in Tables SI3–11.

4. RESULTS

4.1. Detrital samples

4.1.1. Composition

The >63 μm fractions of the Nankai samples are primarily composed of biotite, quartz, and feldspar (Fig. 4); relative composition of samples varies by grain size with biotite being the most common mineral in the coarsest grain sizes; quartz is most common in finer grain sizes. The XRD data indicate that the clay-sized fraction includes quartz, chlorite, biotite, and vermiculite. Quantitative XRD analysis of the <63 μm fractions revealed that both CH-121 and CH-122 are dominated by kaolinite, micas (biotite), quartz, feldspars, and 2:1 clay minerals; they also contain traces of calcite. Differences between the catchments arise from the relative amounts of kaolinite and quartz. Acid extraction dissolved the 2:1 clay minerals and micas (Fig. SI10, Table 1).

The coarse (>63 μm) fractions of the Weiyuan samples are primarily composed of quartz grains, ferruginous fine-grained material, and calcite grains (Fig. 5). The clay-sized minerals include quartz, hematite, and vermiculite. The XRD quantification of the fine (<63 μm) fraction of the Weiyuan samples indicate that the sediment in samples CH-114 and CH-116 is dominated by quartz and micas, with significant amounts of 2:1 clay mineral and plagioclase in CH-114 and kaolinite and illite/smectite in CH-116; both contain traces of goethite. Only CH-114 contained detectable calcite. Amounts of 2:1 clay minerals and calcite decreased after acid extraction in CH-114 while goethite and kaolinite were dissolved by HCl in CH-116 (Fig. SI10, Table 1).

The coarse material in the Vermilion sediments is primarily composed of quartz, feldspar, carbonate, and lithic fragments (Fig. 4). Quantitative XRD analysis of the <63 μm fraction of V-005 and V-007 revealed that these samples are dominated by quartz, micas, and feldspars; both also contain significant amounts of 2:1 clay minerals and kaolinite as well as traces of calcite. The V-007 sample also contains dolomite and amphibole. Post-extraction quantification revealed that most 2:1 clay minerals and carbonate dissolved in the samples (Fig. SI10, Table 1).

For all samples, HCl-extraction tended to remove the calcite and 2:1 clay minerals in addition to crystalline iron hydroxides where present. In samples where dolomite and amphibole were present, these were also removed by the extraction. Considering the HCl-extraction data by element to understand better the composition of dissolved materials, we find that Fe, Mg, Ca, and Mn are preferentially dissolved by the extraction, with over 50% of each element in the leachate, and this finding does not vary by grain size (Fig. 5). Although the percentage of each element that is dissolved by the HCl-leaching does not vary by grain size, the concentration of HCl-extractable material does depend on grain size, such that the highest concentration of HCl-extractable materials were measured in the finest and coarsest grain sizes, with significantly less in the intermediate grain sizes (Fig. 6).

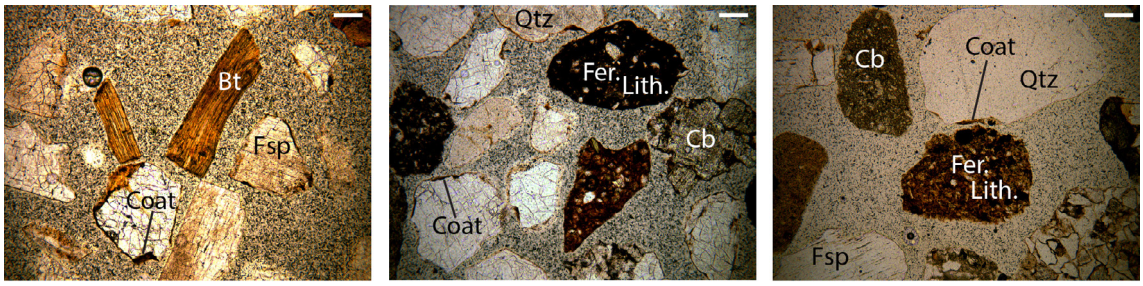

Fig. 4. Thin section micrographs of a 250–500 μm sample from each watershed. Scale bar is 100 μm. Labeled grains include quartz (Qtz), carbonates (Cb), feldspars (Fsp), biotite (Bt), grain coatings (Coat), and ferrigenous lithic fragments (Fer. Lith.). Within each basin, all watersheds are similar. To see micrographs of all grain sizes of each sample, see Figs. SI7–9.

Table 1
Results in weight% of the Rietveld quantitative XRD analysis of the <63 μm fraction of six detrital samples before and after HCl leaching.

	Quartz	Plag.	K-spar	Kaol.	Musc.	2:1 Clay	Illite–smectite	Goethite	Calcite	Dolomite	Amphibole
Weiyuan											
CH-114 pre	51.2	7.3	–	–	25.6	10.4	–	1.1	4.4	–	–
CH-114 post	60.3	5.8	–	–	25.2	7.9	–	0.9	0	–	–
Weiyuan											
CH-116 pre	40.1	–	–	15.2	32.6	–	9.5	2.6	–	–	–
CH-116 post	38.6	–	–	13.6	37.5	–	10.3	0	–	–	–
Nankai											
CH-121 pre	17.5	15	15.6	22.8	21.4	7.2	–	–	0.4	–	–
CH-121 post	3.8	3.3	3.4	70.3	17	1.4	–	–	0.7	–	–
Nankai											
CH-122 pre	10.2	18	1.7	34.4	22	11.6	–	–	2.1	–	–
CH-122 post	8.8	15.9	2.4	45.7	18.5	6.9	–	–	1.7	–	–
Vermilion											
V-005 pre	36.4	9.2	5.9	5	27	14.4	–	–	2.1	–	–
V-005 post	38.1	13.3	3.2	11.5	33.9	0	–	–	0	–	–
Vermilion											
V-007 pre	45.1	9.6	4.6	3.6	19.9	10.6	–	–	3.4	2	1.3
V-007 post	47.3	11.3	7.6	6.4	27.4	0	–	–	0	0	0

4.1.2. Isotope activity

We found measureable activities of $^{10}Be_m$ and $^{210}Pb_{ex}$ in the Yunnan samples (Nankai and Weiyuan Rivers), but did not find measureable ^{137}Cs in any grain size of these samples. We did not detect ^{7}Be ($t_{1/2} = 53$ days) in Yunnan samples likely because of decay during the long waiting time (>1 year, >7 half-lives) between sample collection, overseas shipping, and thus the dates we performed gamma spectrometry. We found detectable ^{7}Be, ^{137}Cs, and $^{210}Pb_{ex}$ in the Ohio samples; we did not measure $^{10}Be_m$ in these samples. At all three sites with detectable ^{7}Be and ^{137}Cs (V-005, V-006, and V-007), ^{7}Be and ^{137}Cs activities were above the detection limit in only the finest fractions (<63 μm) (Fig. 6), with the exception of the 500–850 μm fraction at site V-005, which had a similar ^{7}Be activity as that of the <63 μm fraction.

Grain size exerts a significant control on FRN activity in our samples. $^{10}Be_m$ displayed a pronounced grain-size dependency in the Nankai watershed (CH-121, 122, and 127) with highest activities in the <63 μm fraction, at least a factor of two more than in other grain sizes (Fig. 6). In the Weiyuan samples (CH-114, 116, and 117), $^{10}Be_m$ activity was also highest in the <63 μm fraction, but the difference in activity between grain sizes was less than in the Nankai samples (Fig. 6).

$^{210}Pb_{ex}$ activity was highest in the <63 μm fraction of CH-121; however, at the other two sites in the Nankai watershed (CH-122 & CH-127) there was an apparent reverse grain-size dependency of $^{210}Pb_{ex}$ with higher activity in the coarse fractions. In the Weiyuan watershed, $^{210}Pb_{ex}$ had a higher activity in the fines, although the coarsest fraction at site CH-114 had $^{210}Pb_{ex}$ activity that was within error of the <63 μm fraction (Fig. 6). $^{210}Pb_{ex}$ activity was above the detection limit in almost all grain sizes of the Ohio samples. At sites V-005 and V-006, the $^{210}Pb_{ex}$ activity was highest in the <63 μm fraction, while at site V-007, $^{210}Pb_{ex}$ activity was similar (within error) in the <63 μm and the two coarsest grain sizes (250–500 μm and 500–850 μm) (Fig. 6).

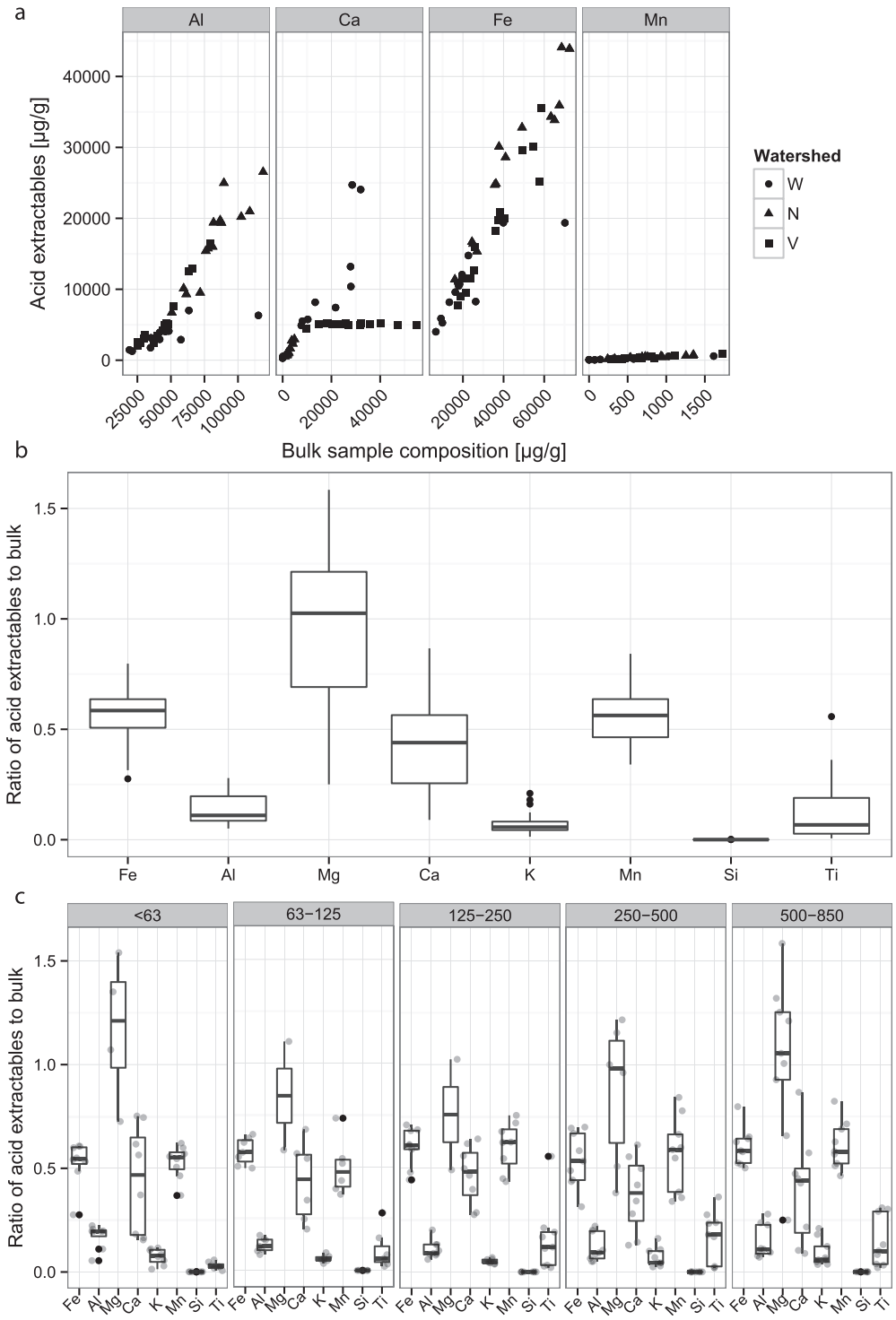

Fig. 5. (a) HCl-extractable material concentration as a function of bulk sample composition. (b) Ratio of elemental concentration in grain coatings (from HCl-leachate) to bulk sample (from pXRF) shows that 50% or more of Fe, Mg, Ca, and Mn are acid-extractable. In each box and whisker plot, the median is the middle line in each box, the 25th and 75th percentiles are the edges of the box, and whiskers extend to include all samples within 1.5 times the range from the 25th to 75th percentiles. Outliers are samples outside that range. (c) The difference in element concentrations in the HCl-extractable materials by grain size. Relative proportions of each element contained in the HCl-extractable material are similar across all grain sizes. Box and whisker definitions are the same as for (b). Gray points behind the boxes show the data contributing to each box. Ratios greater than one are because the ICP-OES analyses are significantly more sensitive than pXRF analyses for light elements; this results in the pXRF concentrations being underestimated for light elements. Thus, for elements that nearly entirely dissolve in the hot HCl-leaches, ratios may appear to be greater than one.

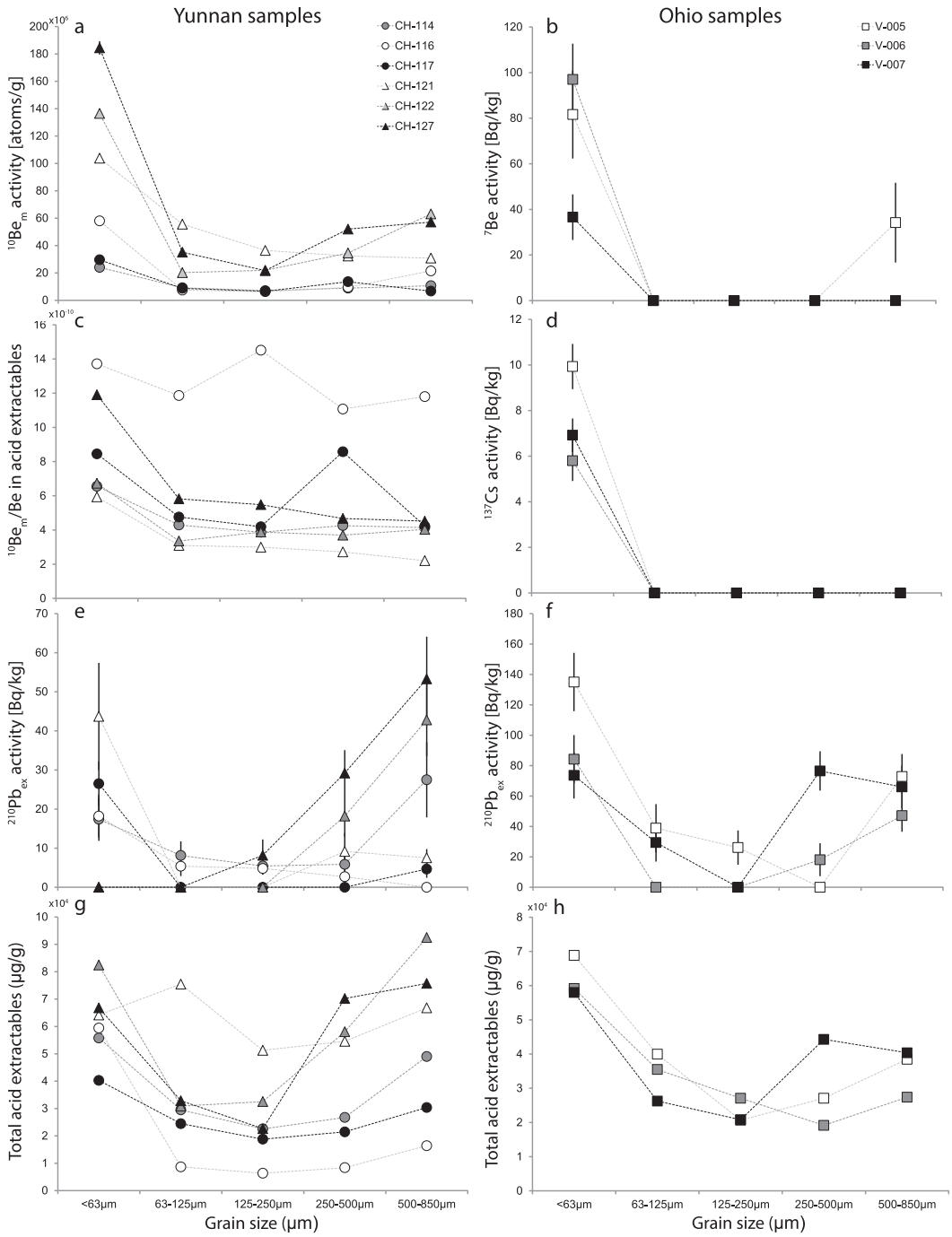

Fig. 6. Activities of FRNs and grain coatings by grain size in the detrital samples. Yunnan samples are plotted as circles (Weiyuan) and triangles (Nankai). Ohio (Vermilion) samples are squares. For each study basin, the smallest basin symbols are the white, intermediate basin symbols are gray, and the largest basin symbols are black. Samples where ^{137}Cs, ^{7}Be, and $^{210}Pb_{ex}$ are below the detection limit are plotted as 0, including those samples where apparent supported ^{210}Pb is greater than total measured ^{210}Pb. (a) The activity of $^{10}Be_m$ for Yunnan samples. (b) The activity of ^{7}Be for Ohio samples. (c) The ratio of $^{10}Be_m$ activity to total Be in the grain coatings for Yunnan samples. (d) The ^{137}Cs activity for Ohio samples. (e, f) The activity of $^{210}Pb_{ex}$ in the Yunnan (e) and Ohio (f) samples. (g, h) The total grain coatings (µg/g) in the Yunnan (g) and Ohio (h) samples.

In all basins, individually and considered as a whole, and across all grain sizes, $^{10}Be_m$ and $^{210}Pb_{ex}$ activity is significantly correlated with the concentration of iron and manganese in the HCl-extractable materials (measured by ICP-OES) as well as the sum of elemental abundances in the HCl-extractable materials ($R^2 \geqslant 0.27$, $p \leqslant 0.05$ for all regressions, Fig. 7). Regressions are significantly better for $^{210}Pb_{ex}$ when considering basins individually than when combining data from all three watersheds. In addition, for $^{210}Pb_{ex}$ in the Vermilion samples and for $^{10}Be_m$ measure-

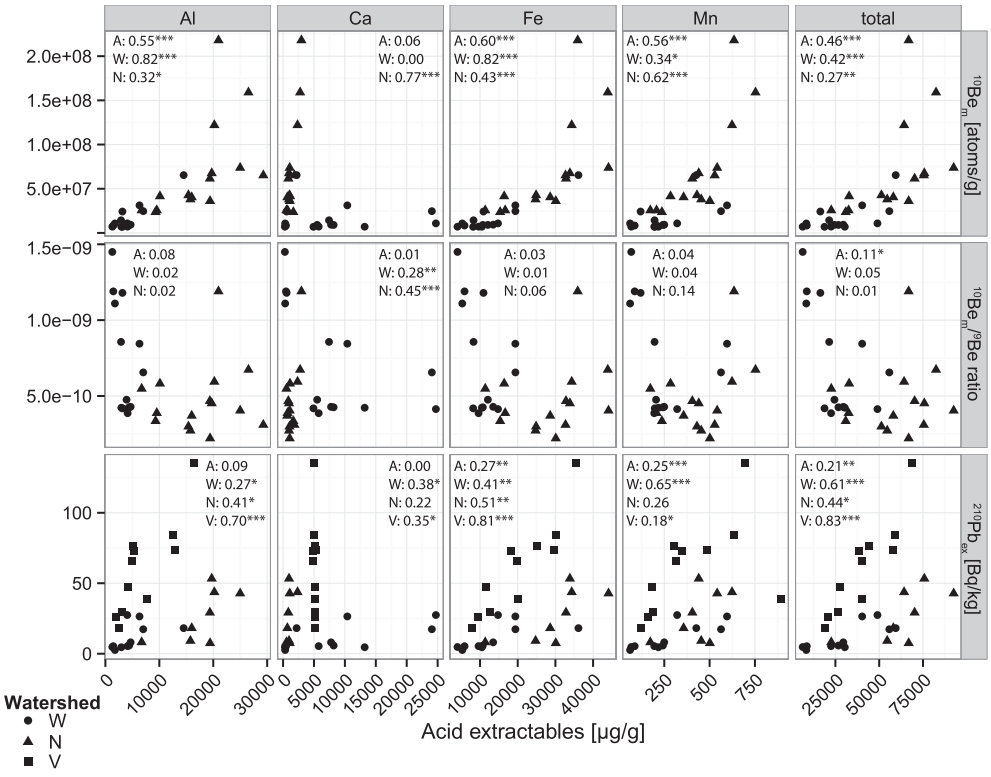

Fig. 7. Scatter plots showing $^{210}Pb_{ex}$, $^{10}Be_m$, and $^{10}Be_m/^9Be$ ratio as a function of major elements in the HCl-leachate (ICP-OES). Samples with $^{210}Pb_{ex}$ below the detection limit or with supported ^{210}Pb greater than total ^{210}Pb are not included in correlations. The bottom row shows the relationship between HCl-leachate concentration of elements and the bulk sample concentration of the same elements. Errors on measurements not shown for clarity. R^2 values are reported in each plot. A = all samples; W = Weiyuan samples; N = Nankai samples, V = Vermilion samples. $^{*}p < 0.10$; $^{**}p < 0.05$; $^{***}p < 0.01$.

ments in both Yunnan basins, considered together and individually, activity is linearly correlated to acid-extractable aluminum concentration ($R^2 \geqslant 0.32$, $p \leqslant 0.05$ for all regressions, Fig. 7). Although $^{10}Be_m$ activity and $^{210}Pb_{ex}$ activity do not correlate with calcium concentration when considering all samples together, for each watershed there is a correlation between calcium and both $^{10}Be_m$ and $^{210}Pb_{ex}$. There are not enough samples with detectable ^7Be or ^{137}Cs to complete regression analysis for these isotopes.

$^{10}Be_m/^9Be$ ratios exhibit grain-size dependency and are generally higher in the <63 µm fractions (Fig. 6), although this is less pronounced than in the $^{10}Be_m$ data. CH-116 has higher $^{10}Be_m/^9Be$ ratios for all grain sizes than the other samples. In addition, the 250–500 µm fraction at CH-117 and the 125–250 µm fraction at site CH-116 have a higher $^{10}Be_m/^9Be$ ratio than expected based on other grain size fractions at the same site. The $^{10}Be_m/^9Be$ ratio only correlates with Ca for basins considered separately ($R^2 \geqslant 0.28$, $p < 0.05$) and, weakly, with total abundance of HCl-extractable materials for both watersheds taken together ($R^2 = 0.11$, $p < 0.10$) (Fig. 7).

4.2. Natural delivery experiment

Most samples exposed to rainfall and dryfall for nearly a year accumulated measurable ^7Be and ^{210}Pb. We did not detect ^{137}Cs. Measurable ^{210}Pb accumulated in 10 of the 15 samples over the course of the entire experiment, with the largest increase in ^{210}Pb in the kaolinite, followed by the <63 µm, 250–500 µm, and 500–850 µm fractions of river sand. Accumulation is approximately within two sigma error for these containers. Illite, montmorillonite, the <63 µm fraction of quartz sand, and the 63–125 µm and 125–250 µm fractions of river sand did not accumulate any ^{210}Pb over the course of the experiment. Between individual time periods, increases in ^{210}Pb were generally too small to be detected reliably. From the start to the end of the experiment, we observed measureable increases in ^7Be activity in every sample with the exception of kaolinite and montmorillonite, which did not retain any measureable ^7Be during any of the five measurement periods or for the experiment as a whole (Fig. 8, Table SI11). Sample mass does not correlate to retention of FRNs at any point in the natural delivery experiment. Data are reported in Bq/m^2, not Bq/kg because samples had different masses of material but container openings were uniform, ensuring that samples were exposed to the same delivery of FRNs.

Retention of ^7Be and $^{210}Pb_{ex}$ showed no grain-size dependency in the five grain sizes of quartz and river sediment, both in changes in activity between consecutive measurements, and in total from start to end of the experiment (Fig. 8). Several samples lost ^7Be beyond the amount calcu-

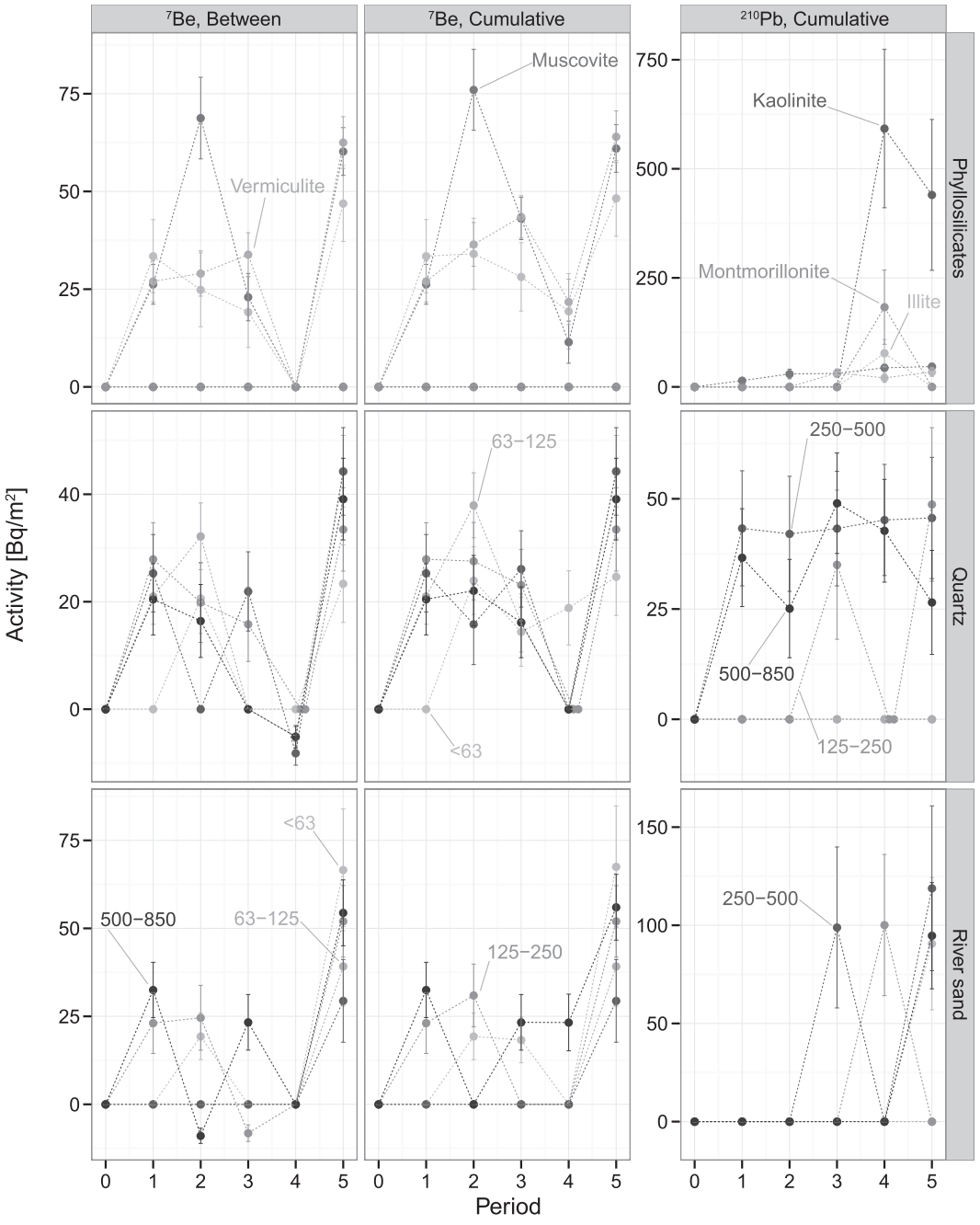

Fig. 8. Results from the natural delivery experiment. The left column shows the results for ^{7}Be between periods, the middle column for cumulative ^{7}Be added during the experiment, and the right for cumulative $^{210}Pb_{ex}$ added during the experiment. The top row shows the data for the phyllosilicates, the middle for the different grain sizes of quartz, and the bottom for the different grain sizes of river sand. ^{7}Be calculations are corrected for decay between measurement periods, so negative amounts show actual loss of ^{7}Be beyond that expected due to decay. One sigma error bars are shown for samples with a net change in activity. We omit error bars for samples with no net change in activity because we have no good way to determine error bars for such a difference.

lated for decay. It is unlikely that this is due to loss of sample because we observed no detectable loss in ^{210}Pb at any point in the experiment. Loss of ^{7}Be appeared to be prevalent after the fourth (and longest) measurement period, but was not systematic. Although containers had varying amounts of material, the increase in activity is not correlated to the amount of material in each sample.

Ratios of HCl-extractable material to bulk sample composition by element suggest that in the river sand samples of the natural delivery experiment, Fe, Mn, and Mg are the primary elements contained in the HCl-extractable materials. However, the phyllosilicates and quartz sand do not have a clear pattern in which elements are HCl-extractable (Fig. SI11). Furthermore, there is no relation-

ship between HCl-extractable materials and activity gained for cumulative or individual time period measurements (Fig. SI12).

5. DISCUSSION

We examined the relative influence of grain size, mineralogy, and the composition and abundance of grain coatings to understand better why and how the grain size dependencies in FRN activity we observed developed. Our experiments suggest that FRN distribution in sediment is a time-dependent function of sample composition, particularly the amount of HCl-extractable materials and grain size. The difference in distribution of FRNs by grain size and HCl-extractable composition in the natural delivery experiment and the detrital sediments suggests that pedogenic processes happening in the soil, and possibly related to organic matter (c.f., Smith and Blake, 2014) affect adsorption of FRNs to soil, which then erodes and becomes sediment. Furthermore, the strong correlation between the amount of HCl-extractable material in the detrital samples and the FRN activity of these samples is consistent with the conclusion that the concentration of reactive materials and their composition are a primary control on FRN activity, rather than substrate lithology or sample grain size alone; however, we realize that concentration of reactive coatings, lithology, and grain size likely co-vary. We are unable to draw any conclusions regarding ^{137}Cs and ^{7}Be in detrital samples due to the small number of samples with detectable activity of these isotopes. We hypothesize that the Yunnan samples do not have any detectable ^{137}Cs due to extensive erosion during the time of ^{137}Cs deposition (Neilson, 2015) and thus are sourcing material that was too deep to receive ^{137}Cs fallout (e.g., Olley et al., 2013).

In this discussion, in addition to exploring the role of HCl-extractable materials as a proxy for pedogenic grain coatings in FRN distribution (Greene, 2016), we consider the implications of our findings for normalizing $^{10}Be_m$ measurements by ^{9}Be, possible problems with standard methods for determining $^{210}Pb_{ex}$ activity, and the relative importance of specific surface area and substrate lithology in FRN distribution.

5.1. Control of FRN distribution by HCl-extractable materials

The composition of materials extracted by the hot HCl suggests that this process targets secondary minerals produced during pedogenesis. As we observed, hot hydrochloric acid extraction dissolves iron oxides, carbonates, and 2:1 clay minerals, and leaves quartz, feldspars, and, to a lesser extent, micas undissolved. We do not attribute the apparent loss of quartz in CH-121 after acid-extraction to dissolution, but rather to the uncertainty in the quartz particle size modeling for the Reitveld analysis (Table 1). Therefore, we assume that the composition of HCl-extractable materials is a proxy for the composition of reactive grain coatings in samples and associated sorbed cations (Greene, 2016). Considering individual elements in the HCl-extracted leachate, we find that HCl-extraction dissolves large fractions of Fe, Mg, Ca and Mn (Fig. 5b), suggesting that reactive grain coatings are composed of these minerals. The large concentrations of Fe leached from the sediments (Fig. 5a) suggest that amorphous Fe oxy-hydroxides are a significant component of reactive grain coatings (e.g., Wittmann et al., 2012). With the exception of Mg, the ratio of HCl-extractable materials to bulk composition of samples, and thus grain coating composition, is relatively uniform across all grain sizes (Fig. 5c). The increase in Mg in HCl-extractable materials in the <63 μm fraction of all samples is likely due to enrichment of clay minerals in this size.

We find that the activity of fallout radionuclides is strongly correlated to the mass and composition of the HCl-extractable materials for detrital samples. In contrast, FRN activity does not correlate with the mass and composition of HCl-extractable materials in the natural delivery experiments, which, except for the river sediments, lack grain coatings. For detrital samples, $^{10}Be_m$ correlates with HCl-extractable materials when considering the entire dataset (Fig. 7). In contrast, $^{210}Pb_{ex}$ correlations with HCl-extractable materials improve when considering the watersheds individually. In particular, our data support the suggestion that $^{10}Be_m$ is associated with reactive phases, including iron oxides, both crystalline and amorphous (Wittmann et al., 2012). This suggests the importance of time-dependent pedogenic processes in remobilizing and retaining $^{10}Be_m$ over timescales longer than the residence time of $^{210}Pb_{ex}$ in the system. The lack of correlation between any HCl-extractable materials and isotope activity in the natural delivery experiment suggests the importance of time-dependent processes and grain coatings in retaining even short-lived isotopes, such as $^{210}Pb_{ex}$.

5.2. Effect of Be normalization

Although normalizing $^{10}Be_m$ by ^{9}Be in the HCl-leachate is proposed as a way to remove the effects of preferential distribution due to grain size differences (Wittmann et al., 2012), we find that normalizing $^{10}Be_m$ activity by ^{9}Be reduces but does not eliminate grain-size dependencies, with higher ratios in the <63 μm fraction than in other fractions (Fig. 6). This suggests that normalizing $^{10}Be_m$ data by ^{9}Be may not remove all the effects of preferential adsorption of $^{10}Be_m$, particularly among different grain sizes and geologic settings.

5.3. Inconsistencies in ^{210}Pb activity

The measurement accuracy of $^{210}Pb_{ex}$ in detrital sediments is problematic. For some samples, the activity of $^{210}Pb_{ex}$ decreases with decreasing grain size, while the activity of total ^{210}Pb and supported ^{210}Pb as well as concentration of HCl-extractable materials increases (Fig. 6, Fig. SI13, Table SI10). In addition, for some of these samples, apparent supported ^{210}Pb activity is significantly greater than total ^{210}Pb, which is not possible, and in core samples, would be attributed to radon leakage (Graustein and Turekian, 1990; Greeman and Rose, 1996; Du and Walling, 2012). Furthermore, the order of magnitude variation in supported ^{210}Pb in each of the Vermilion

and Nankai watershed samples is surprising given that supported ^{210}Pb should reflect the bedrock contributing sediment to a given sample. We suggest that the large variations in supported ^{210}Pb in the Nankai and Vermilion watersheds are the reason for the decrease in $^{210}Pb_{ex}$ activity with decreasing grain sizes.

The unusual pattern in the supported ^{210}Pb activity may be due to overestimating supported ^{210}Pb within the grains because we are including all ^{222}Rn produced as well as materials associated with grain coatings and adsorbed to grains as part of our supported ^{210}Pb estimate. In other words, we are not accounting for radon leakage (Graustein and Turekian, 1990; Greeman and Rose, 1996; Du and Walling, 2012). This could happen if ^{226}Ra ejected from the grains by alpha recoil then becomes adsorbed to grains or otherwise associated with grain coatings or when ^{222}Rn is ejected from grains by alpha recoil (Fig. SI5). The tendency we have observed for other materials to be preferentially associated with fine grain sizes would likely hold true for ^{226}Ra as well, thus increasing the overestimation of supported ^{210}Pb in the fine grain sizes. A potentially interesting area of future research is to test whether HCl-extractable materials do contain ^{226}Ra. If this is true, it could mean that measuring $^{210}Pb_{ex}$ in only the <63 μm fraction could lead to significant underestimates of $^{210}Pb_{ex}$.

5.4. Does mineralogy or specific surface area control FRN distribution?

Prior research investigating preferential distribution of FRNs in fine sediment has suggested that this effect is due either to the higher specific surface area of fine sediments (He and Walling, 1996; Wittmann et al., 2012; Taylor et al., 2014) or because fine sediments are enriched in minerals with higher surface charges to which FRNs can better sorb (Tamura, 1963; Aldahan et al., 1999; Nakao et al., 2014). Our detrital sample results show that FRNs are associated with acid-extractable phases and that these are predominantly iron oxides, clay minerals, and carbonates; in contrast, we do not find this association for the exposure experiment samples, which are largely devoid of pedogenic coatings. If specific surface area of the minerals were the primary control on FRN distribution, montmorillonite (a high SSA clay) and finer fractions of quartz and river sand would have higher ^{7}Be and ^{210}Pb concentrations than other samples at all time periods of the natural delivery experiment. However, we observe: (1) kaolinite (lower SSA) has the highest ^{210}Pb retention potential among clays, but never retained ^{7}Be (Fig. 8); (2) vermiculite, illite, and muscovite have similar ^{7}Be retention potential while kaolinite and montmorillonite never retained ^{7}Be (Fig. 8); (3) $^{10}Be_{m}$ is strongly correlated with a few elements during acid leaching (Fig. 7); and, (4) medium grain size samples (63–125 μm and 125–250 μm) have the lowest concentration of HCl-extractable materials as well as the lowest activity of $^{210}Pb_{ex}$ and $^{10}Be_{m}$ in most samples (Fig. 6). We suggest, therefore, that the presence and amount of HCl-extractable materials is more important than either specific surface area or surface charge in setting the distribution of FRNs. Furthermore, the concentration of HCl-extractable material is related to grain size such that medium grain size fractions have the lowest concentrations.

6. CONCLUSIONS

We find that the concentration of HCl-extractable materials is a stronger control on distribution of FRNs in samples than either the grain size or the mineralogy of samples. In addition, we find significant differences between distribution of FRNs in a controlled natural delivery experiment and detrital river samples, suggesting that pedogenic coatings present in natural settings, but not our natural delivery experiment, are a key factor in adsorption of FRNs. The correlation between HCl-extractable materials and FRN concentration suggests that FRN adsorption sites are likely associated with grain coatings. Grain coating composition and abundance is more important than either grain size or mineralogy in setting rates of FRN adsorption to sediment samples.

ACKNOWLEDGEMENTS

Research supported by NSF EAR-1114166 (to Schmidt), EAR-1114159 (to Bierman), and EAR-1114436 (to Rood), and the State Key Laboratory Open Fund (China). Oberlin XRD was funded by NSF DMR-0922588 (to Dr. Catherine Oertel). UVM XRD was funded by NSF EAR-0922961 (to Dr. John Hughes). We thank V. Sosa-Gonzalez, Y. Qiu, and S. Woodmansee for help with fieldwork, M. Campbell for assistance with implementation of the natural-delivery experiment and with fieldwork, J. Martin for GIS mapping, N. McMillion for assistance with creating thin sections, the staff of SUERC for support during AMS measurements, and three anonymous reviewers for constructive feedback that improved the manuscript considerably.

APPENDIX A. SUPPLEMENTARY DATA

Supplementary data associated with this article can be found, in the online version, at http://dx.doi.org/10.1016/j.gca.2016.10.007.

REFERENCES

Aldahan A., Ye H. P. and Possnert G. (1999) Distribution of beryllium between solution and minerals (biotite and albite) under atmospheric conditions and variable pH. *Chem. Geol.* **156**, 209–229.

Appleby P. G., Nolan P. J., Gifford D. W., Godfrey M. J., Oldfield F., Anderson N. J. and Battarbee R. W. (1986) Pb-210 dating by low background gamma-counting. *Hydrobiologia* **143**, 21–27.

Bacon A. R., Richter D. D., Bierman P. R. and Rood D. H. (2012) Coupling meteoric Be-10 with pedogenic losses of Be-9 to improve soil residence time estimates on an ancient North American interfluve. *Geology* **40**, 847–850.

Barg E., Lal D., Pavich M. J., Caffee M. W. and Southon J. R. (1997) Beryllium geochemistry in soils: evaluation of ^{10}Be/^{9}Be ratios in authigenic minerals as a basis for age models. *Chem. Geol.* **140**, 237–258.

Belmont P., Willenbring J. K., Schottler S. P., Marquard J., Kumarasamy K. and Hemmis J. M. (2014) Toward generalizable sediment fingerprinting with tracers that are conservative

and nonconservative over sediment routing timescales. *J. Soils Sediments* **14**, 1479–1492.
Bhat P. N., Soundararajan S. and Ghosh D. K. (2005) Studies on chemical analogy of calcium and beryllium in soil. *Indian J. Chem. Technol.* **12**, 534–538.
Brown L., Pavich M. J., Hickman R. E., Klein J. and Middleton R. (1988) Erosion of the eastern United States observed with Be-10. *Earth Surf. Processes* **13**, 441–457.
Covelo E. F., Vega F. A. and Andrade M. L. (2007) Competitive sorption and desorption of heavy metals by individual soil components. *J. Hazard. Mater.* **140**, 308–315.
Dietrich W. E., Dunne T., Humphrey N. F. and Reid L. M. (1982) Construction of sediment budgets for drainage basins. In *Sediment Budgets and Routing in Forested Drainage Basins: Proceedings of the Symposium 1*, pp. 5–23.
Downs R. T. and Hall-Wallace M. (2003) The American Mineralogist crystal structure database. *Am. Mineral.* **88**, 247–250.
Du P. and Walling D. (2012) Using ^{210}Pb measurements to estimate sedimentation rates on river floodplains. *J. Environ. Radioact.* **103**, 59–75.
Fuller A. J., Shaw S., Peacock C. L., Trivedi D., Small J. S., Abrahamsen L. G. and Burke I. T. (2014) Ionic strength and pH dependent multi-site sorption of Cs onto a micaceous aquifer sediment. *Appl. Geochem.* **40**, 32–42.
Gilmore G. R. (2011) *Practical Gamma-ray Spectrometry*. John Wiley & Sons, West Sussex, England.
Graly J. A., Bierman P. R., Reusser L. J. and Pavich M. J. (2010) Meteoric ^{10}Be in soil profiles – a global meta-analysis. *Geochim. Cosmochim. Acta* **74**, 6814–6829.
Graustein W. C. and Turekian K. K. (1990) Radon fluxes from soils to the atmosphere measured by ^{210}Pb–^{226}Ra disequilibrium in soils. *Geophys. Res. Lett.* **17**, 841–844.
Gražulis S., Chateigner D., Downs R. T., Yokochi A. T., Quirós M., Lutterotti L., Manakova E., Butkus J., Moeck P. and Le Bail A. (2009) Crystallography open database – an open-access collection of crystal structures. *J. Appl. Crystallogr.* **42**, 726–729.
Gražulis S., Daškevič A., Merkys A., Chateigner D., Lutterotti L., Quirós M., Serebryanaya N. R., Moeck P., Downs R. T. and LeBail A. (2012) Crystallography Open Database (COD): an open-access collection of crystal structures and platform for world-wide collaboration. *Nucleic Acids Res.* **40**, D420–D427.
Greeman D. J. and Rose A. W. (1996) Factors controlling the emanation of radon and thoron in soils of the eastern USA. *Chem. Geol.* **129**, 1–14.
Greene E. S. (2016) *Comparing Meteoric ^{10}Be, in situ ^{10}Be, and native ^{9}Be across a diverse set of watersheds, Geology*. University of Vermont, Burlington, VT, p. 118.
Guzmán G., Quinton J. N., Nearing M. A., Mabit L. and Gómez J. A. (2013) Sediment tracers in water erosion studies: current approaches and challenges. *J. Soils Sediments* **13**, 816–833.
Hancock G. J., Wilkinson S. N., Hawdon A. A. and Keen R. J. (2014) Use of fallout tracers ^{7}Be, ^{210}Pb and ^{137}Cs to distinguish the form of sub-surface soil erosion delivering sediment to rivers in large catchments. *Hydrol. Processes* **28**, 3855–3874.
He Q. and Walling D. E. (1996) Interpreting particle size effects in the adsorption of ^{137}Cs and unsupported ^{210}Pb by mineral soils and sediments. *J .Environ. Radioact.* **30**, 117–137.
Henck A., Huntington K. W., Stone J. O., Montgomery D. R. and Hallet B. (2011) Spatial controls on erosion in the Three Rivers Region, southwest China. *Earth Planet. Sci. Lett.* **303**, 71–83.
Hooke R. L. (2000) On the history of humans as geomorphic agents. *Geology* **28**, 843–846.
Ioannidou A. and Papastefanou C. (2006) Precipitation scavenging of ^{7}Be and ^{137}Cs radionuclides in air. *J. Environ. Radioact.* **85**, 121–136.
Jia G., Belli M., Liu S., Sansone U., Xu C., Rosamilia S., Xiao X., Gaudino S., Chen L. and Yang H. (2006) The fractionation and determination procedures for the speciation of ^{210}Pb and ^{210}Po in soil samples. *Anal. Chim. Acta* **562**, 51–58.
Jovanovic S., Dlabac A. and Mihaljevic N. (2010) ANGLE v2.1-new version of the computer code for semiconductor detector gamma-efficiency calculations. *Nucl. Instrum. Methods Phys. Res., Sect. A* **622**, 385–391.
Kaste J. M., Magilligan F. J., Renshaw C. E., Fisher G. B. and Dade W. B. (2014) Seasonal controls on meteoric Be-7 in coarse-grained river channels. *Hydrol. Processes* **28**, 2738–2748.
Kristiansen N. I., Stohl A. and Wotawa G. (2012) Atmospheric removal times of the aerosol-bound radionuclides ^{137}Cs and ^{131}I measured after the Fukushima Dai-ichi nuclear accident – a constraint for air quality and climate models. *Atmos. Chem. Phys.* **12**, 10759–10769.
Landis J. D., Renshaw C. E. and Kaste J. M. (2012) Measurement of ^{7}Be in soils and sediments by gamma spectroscopy. *Chem. Geol.* **291**, 175–185.
Likuku A. S. and Branford D. (2011) Deposition rates of atmospheric particulates determined from ^{210}Pb measurements in soils and air. *Pol. J. Environ. Stud.* **20**, 405–410.
Mabit L., Benmansour M. and Walling D. E. (2008) Comparative advantages and limitations of the fallout radionuclides Cs-137, Pb-210(ex) and Be-7 for assessing soil erosion and sedimentation. *J. Environ. Radioact.* **99**, 1799–1807.
Mabit L., Meusburger K., Fulajtar E. and Alewell C. (2013) The usefulness of Cs-137 as a tracer for soil erosion assessment: a critical reply to Parsons and Foster (2011). *Earth Sci. Rev.* **127**, 300–307.
Matisoff G. and Whiting P. J. (2012) Measuring soil erosion rates using natural (^{7}Be, ^{210}Pb) and anthropogenic (^{137}Cs, ^{239}, ^{240}Pu) radionuclides. In *Handbook of Environmental Isotope Geochemistry* (ed. M. Baskaran). Springer, pp. 487–519.
Moore D. M. and Reynolds R. C. (1997) *X-ray Diffraction and the Identification and Analysis of Clay Minerals*. Oxford University Press, Oxford.
Murray A. S., Marten R., Johnston A. and Martin P. (1987) Analysis for naturally-occurring radionuclides at environmental concentrations by gamma spectrometry. *J. Radioanal. Nucl. Chem. Art.* **115**, 263–288.
Nakao A., Ogasawara S., Sano O., Ito T. and Yanai J. (2014) Radiocesium sorption in relation to clay mineralogy of paddy soils in Fukushima, Japan. *Sci. Total Environ.* **468–469**, 523–529.
Neilson T. B. (2015) *Using Long- and Short-Lived Sediment-Associated Isotopes to Track Erosion and Sediment Movement Through Rivers in Yunnan, SW China, Geology*. University of Vermont, Burlington, VT, p. 175.
Nishiizumi K., Imamura M., Caffee M. W., Southon J. R., Finkel R. C. and McAninch J. (2007) Absolute calibration of ^{10}Be AMS standards. *Nucl. Instrum. Methods Phys. Res., Sect. B* **258**, 403–413.
Olley J., Brooks A., Spencer J., Pietsch T. and Borombovits D. (2013) Subsoil erosion dominates the supply of fine sediment to rivers draining into Princess Charlotte Bay, Australia. *J. Environ. Radioact.* **124**, 121–129.
Ouimet W., Dethier D., Bierman P., Wyshnytzky C., Shea N. and Rood D. H. (2015) Spatial and temporal variations in meteoric ^{10}Be inventories and long-term deposition rates, Colorado Front Range. *Quatern. Sci. Rev.* **109**, 1–12.
Papastefanou C. and Ioannidou A. (1996) Beryllium-7 aerosols in ambient air. *Environ. Int.* **22**, 125–130.
Parsons A. J. and Foster I. D. L. (2011) What can we learn about soil erosion from the use of ^{137}Cs? *Earth Sci. Rev.* **108**, 101–113.

Parsons A. J. and Foster I. D. L. (2013) The assumptions of science. A reply to Mabit et al. (2013). *Earth Sci. Rev.* **127**, 308–310.

Reiners P. W., Ehlers T. A., Mitchell S. G. and Montgomery D. R. (2003) Coupled spatial variations in precipitation and long-term erosion rates across the Washington Cascades. *Nature* **426**, 645–647.

Reusser L. J. and Bierman P. R. (2010) Using meteoric ^{10}Be to track fluvial sand through the Waipaoa River basin, New Zealand. *Geology* **38**, 47–50.

Seo D. C., Yu K. and DeLaune R. D. (2008) Comparison of monometal and multimetal adsorption in Mississippi River alluvial wetland sediment: Batch and column experiments. *Chemosphere* **73**, 1757–1764.

Smith H. G. and Blake W. H. (2014) Sediment fingerprinting in agricultural catchments: a critical re-examination of source discrimination and data corrections. *Geomorphology* **204**, 177–191.

Snape I., Scouller R. C., Stark S. C., Stark J., Riddle M. J. and Gore D. B. (2004) Characterisation of the dilute HCl extraction method for the identification of metal contamination in Antarctic marine sediments. *Chemosphere* **57**, 491–504.

Sosa-Gonzalez V., Schmidt A. H., Bierman P. R., Neilson T. B., Singleton A., Qiu Y., Bower J. A. and Rood D. H. (2015) Understanding sediment sourcing and erosion controls from ^{10}Be measurements in fluvial sediments from Yunnan, China. *Geol. Soc. Am. Abstr. Programs* **47**, 240.

Srivastava P., Singh B. and Angove M. (2005) Competitive adsorption behavior of heavy metals on kaolinite. *J. Colloid Interface Sci.* **290**, 28–38.

Steefel C. I., Carroll S., Zhao P. H. and Roberts S. (2003) Cesium migration in Hanford sediment: a multisite cation exchange model based on laboratory transport experiments. *J. Contam. Hydrol.* **67**, 219–246.

Stone J. (1998) A rapid fusion method for separation of beryllium-10 from soils and silicates. *Geochim. Cosmochim. Acta* **62**, 555–561.

Stoops G., Marcelino V. and Mees F. (2010) *Micromorphological Features and Their Relation to Processes and Classification, Interpretation of Micromorphological Features of Soils and Regoliths*. Elsevier, Amsterdam, pp. 15–35.

Tamura T. (1963) Cesium sorption reaction as indicator of clay mineral structures. *Clays Clay Miner.*, 389–398.

Taylor A., Blake W. H. and Keith-Roach M. J. (2014) Estimating Be-7 association with soil particle size fractions for erosion and deposition modelling. *J. Soils Sediments* **14**, 1886–1893.

USGS (2001) *Separation of the Silt and Clay Fractions for X-ray Powder Diffraction by Centrifugation, A Laboratory Manual for X-ray Powder Diffraction*. U.S. Geological Survey.

von Blanckenburg F., Bouchez J. and Wittmann H. (2012) Earth surface erosion and weathering from the ^{10}Be (meteoric)/^{9}Be ratio. *Earth Planet. Sci. Lett.* **351–352**, 295–305.

Wallbrink P. J. and Murray A. S. (1993) Use of fallout radionuclides as indicators of erosion processes. *Hydrol. Processes* **7**, 297–304.

Walling D. E., He Q. and Blake W. (1999) Use of ^{7}Be and ^{137}Cs measurements to document short- and medium-term rates of water-induced soil erosion on agricultural land. *Water Resour. Res.* **35**, 3865–3874.

Willenbring J. K. and von Blanckenburg F. (2010) Meteoric cosmogenic Beryllium-10 adsorbed to river sediment and soil: applications for Earth-surface dynamics. *Earth Sci. Rev.* **98**, 105–122.

Wittmann H., Von Blanckenburg F., Bouchez J., Dannhaus N., Naumann R., Christl M. and Gaillardet J. (2012) The dependence of meteoric ^{10}Be concentrations on particle size in Amazon River bed sediment and the extraction of reactive ^{10}Be/^{9}Be ratios. *Chem. Geol.* **318–319**, 126–138.

Xu S., Dougans A. B., Freeman S. P. H. T., Schnabel C. and Wilcken K. M. (2010) Improved ^{10}Be and ^{26}Al-AMS with a 5MV spectrometer. *Nucl. Instrum. Methods Phys. Res., Sect. B* **268**, 736–738.

Xu S., Freeman S. P. H. T., Rood D. H. and Shanks R. P. (2015) Decadal ^{10}Be, ^{26}Al and ^{36}Cl QA measurements on the SUERC 5 MV accelerator mass spectrometer. *Nucl. Instrum. Methods Phys. Res., Sect. B* **361**, 39–42.

Zeitler P. K., Meltzer A. S., Koons P. O., Craw D., Hallet B., Chamberlain C. P., Kidd W. S. F., Park S. K., Seeber L., Bishop M. and Shroder J. (2001) Erosion, Himalayan geodynamics, and the geomorphology of metamorphism. *GSA Today* **11**, 4–9.

Associate editor: Anthony Dosseto